Remote Sensing of Environment 295 (2023) 113705

Contents lists available at ScienceDirect

Remote Sensing of Environment

journal homepage: www.elsevier.com/locate/rse

Spatial and temporal differences in surface and subsurface meltwater distribution over Greenland ice sheet using multi-frequency passive microwave observations

Andreas Colliander[a,*], Mohammad Mousavi[a], John S. Kimball[b], Julie Z. Miller[c], Mariko Burgin[a]

[a] Jet Propulsion Laboratory, California Institute of Technology, Pasadena, CA, USA
[b] University of Montana, Missoula, MT, USA
[c] Cooperative Institute for Research in Environmental Sciences (CIRES), Boulder, CO, USA

ARTICLE INFO

Edited by Dr. Menghua Wang

Keywords:
Ice sheet
Snow
Firn
Melt

ABSTRACT

Increasingly larger portions of the Greenland ice sheet are undergoing seasonal melting-refreeze cycles due to global climate warming. The cycle begins with the arrival of high temperatures and increased solar radiation in the spring and summer seasons generating meltwater on the ice sheet's surface. Meltwater percolates to deeper ice layers, either refreezing within the firn, creating longer-term meltwater pockets (firn aquifers), or generating peripheral runoff. Depending on the location and climate, the refreeze duration, the depth of infiltration, and meltwater persistence are temporally and spatially complex. Our recent study showed that multi-frequency passive microwave measurements in the 1.4 GHz to 36.5 GHz range effectively distinguished seasonal meltwater between the immediate surface and deeper firn layers at an experiment site in the accumulation zone of the southwestern Greenland ice sheet. Here, we further explored the vertically and horizontally polarized multi-frequency melt response at the pan-Greenland scale. We employed 1.4 GHz brightness temperature (TB) measurements from the NASA Soil Moisture Active Passive (SMAP) satellite and 6.9, 10.7, 18.9, and 36.5 GHz TB measurements from the JAXA Global Change Observation Mission-Water Shizuku (GCOM-W) satellite. The results show that the frequency-dependent response was consistent across the ice sheet. The multi-frequency melt indications match with lasting seasonal subsurface meltwater with delayed refreezing compared to the surface. These results suggest persistent seasonal subsurface meltwater occurrences that are spatially and temporally significant but concealed from the high-frequency observations. Retrieving the meltwater evolution in snow and firn presents a complex problem; this work represents an initial step toward developing an ice-sheet-wide algorithm for more comprehensive retrieval of the meltwater profile.

1. Introduction

Passive microwave observations are used for detecting ice sheet melt conditions because of their sensitivity to the permittivity changes in the ice sheet's upper layers during seasonal melt events (e.g., Abdalati and Steffen, 1995; Colosio et al., 2021). Currently operating spaceborne microwave radiometers offer coverage of the polar ice sheets multiple times a day regardless of atmospheric conditions due to their low susceptibility to the effects of clouds, aerosols, and solar illumination. Consequently, these observations yield reliable time series of melt signatures at a spatial resolution of 10–40 km (e.g., Fettweis et al., 2006; Tedesco, 2007). The retrieval techniques have traditionally employed 18.7 GHz and 37 GHz channels (Jezek et al., 1993; Steffen et al., 1993; Mote and Anderson, 1995).

Although the current approaches have helped to make substantial advances in observing the ice sheet melt timing and extent, the limitations of the current observational methods do not allow us to form a complete view of the melt-refreeze dynamics. For example, studies in the Greenland ice sheet percolation zone have shown highly variable seasonal meltwater infiltration with depths of more than 10 m commonplace with spatially variable refreezing timing (e.g., Harper et al., 2012; Cox et al., 2015). The products based on the 18.7 GHz and

---

* Corresponding author.
E-mail address: andreas.colliander@jpl.nasa.gov (A. Colliander).

https://doi.org/10.1016/j.rse.2023.113705
Received 20 September 2022; Received in revised form 26 May 2023; Accepted 26 June 2023

37 GHz brightness temperature (TB) correspond only to the meltwater presence in the top layer of the ice sheet (up to 1 m) and do not carry knowledge on the meltwater refreeze occurring after the meltwater has percolated deeper into the ice sheet (e.g., Tedesco, 2015). This is because the radiation emanating from the deeper layers is suppressed by overlying layers, and the near-surface snow and firn layers provide the dominant satellite signal at these frequencies. Recent studies have explored the 1.4 GHz TB sensitivity to snow liquid water content (LWC) in glaciers using ESA's SMOS (Soil Moisture Ocean Salinity) mission (launched in 2009; Mecklenburg et al., 2016; Houtz et al., 2019) and tower-based measurements (Naderpour et al., 2021) as well as in seasonal snow cover (Naderpour et al., 2017; Naderpour and Schwank, 2018; Schwank and Naderpour, 2018). The studies indicate equivocally that despite the transparency of dry snow at the 1.4 GHz band, it is sensitive to LWC over a range of depths. Moreover, the signal does not saturate with low LWC amounts as it does for the higher frequencies, which enables not only the detection of LWC but also its amount. The 1.4 GHz observations from SMOS and NASA's Soil Moisture Active Passive (SMAP) mission (launched in 2015) (Entekhabi et al., 2010) have been introduced for ice sheet-wide detection of meltwater (Leduc-Leballeur et al., 2020; Houtz et al., 2021; Mousavi et al., 2021, 2022). Furthermore, as the 1.4 GHz radiation penetrates dry snow with little effect, the L-band frequency has also been applied for detecting firn saturation (Miller et al., 2022b), and meltwater stored in deeper perennial firn aquifers (Miller et al., 2020, 2022a). Colliander et al. (2022) showed that the 1.4, 6.9, 10.7, 18.7, and 36 GHz frequency bands could complement each other for retrieving information on the vertical profile of LWC in snow/firn layers over the DYE-2 experiment site in Greenland (Samimi et al., 2020; Samimi et al., 2021). The study used combined multi-frequency TB measurements from SMAP and the Advanced Microwave Scanning Radiometer 2 (AMSR2) onboard the Global Change Observation Mission-Water Shizuku (GCOM-W1) satellite (Imaoka et al., 2010), along with an LWC model calibrated using in situ measurements.

Most traditional melt detection algorithms using 18.9 GHz and 36.5 GHz frequency bands are based on change detection classification of the increased TB that occurs during melt events relative to frozen winter conditions; the approaches vary based on how they define the frozen winter reference and the threshold for melt detection (e.g., Tedesco, 2009). Mousavi et al. (2021, 2022) presented an empirical melt detection algorithm for L-band (1.4 GHz) using a similar change detection approach. This study investigated the multi-frequency TB response to seasonal surface melting at the pan-Greenland scale. Our objective was to clarify the value of combined lower and higher frequency observations for delineating surface melt patterns relative to more traditional assessments involving only higher frequency data. We analyzed the SMAP and AMSR2 TB measurements with air temperature data from selected weather stations. We employed a change detection approach across the 1.4, 6.9, 10.7, 18.9, and 36.5 GHz frequencies using the SMAP and AMSR2 measurements and compared the extent and timing of the melt indications between frequencies. We used the period from 2016 to 2019, which is too short to systematically analyze interannual variations or trends, even if more recent years (2020−2021) were included. Additional L-band data are available from the ESA Soil Moisture and Ocean Salinity (SMOS) mission (starting in 2010), and more C- to Ka-band data are available from the JAXA Advanced Microwave Scanning Radiometer-Earth Observing System (AMSR-E) instrument on the NASA Aqua satellite (extending from 2002 to 2011). However, the 2016–2019 period is adequate for showing the value of the multi-frequency measurements, while the exploitation of the longer time series is left to future studies.

2. Data

2.1. SMAP data

The SMAP L-band radiometer measures vertical (V) and horizontal (H) polarized 1.4 GHz TB with native 38-km resolution sampled from a 6 AM/PM equatorial crossing sun-synchronous orbit (Entekhabi et al., 2014; Piepmeier et al., 2017). The conically scanning, 40° incidence angle, TB measurement results in a 1000-km swath width that allows the measurement of the entire Greenland ice sheet twice daily. The SMAP mission started science data production on March 31, 2015. Here we used the spatially enhanced TB product (L1CTBE, version 3) posted to a consistent 9-km Equal-Area Scalable Earth grid version 2 (EASE2) (Brodzik et al., 2012, 2014) polar grid (Chaubell et al., 2020).

2.2. AMSR data

The AMSR2 instrument provides simultaneous V and H polarized TB measurements at 6.9/7.3 GHz, 10.65 GHz, 18.7 GHz, 23.8 GHz, 36.5 GHz, and 89.0 GHz frequency channels with a 1:30 AM/PM equatorial crossing sun-synchronous orbit (Imaoka et al., 2010). The 3 dB footprint varies with channel frequency, ranging from ~41 km (6.9 GHz) to ~8 km (36.5 GHz) and ~ 5 km (89 GHz). The conically scanning, 55° incidence angle measurement results in about 1900-km swath width that is spatially overlapping with SMAP observations and also allows the measurement of the entire Greenland ice sheet at least twice a day. The AMSR2 mission has produced science data since May 18, 2012. The data were gridded using inverse distance weighting on the same 9-km EASE2 grid as the SMAP data.

2.3. Focus transect

For comparisons with the satellite observations, we used automatic weather station (AWS) data collected along the K-transect near Kangerlussuaq in west Greenland (Fausto et al., 2021). The transect runs from east to west, roughly perpendicular to the ice sheet edge at about 67°N (e.g., Smeets et al., 2018). The K-transect was established originally for the Greenland Ice Margin Experiments (GIMEX) conducted during the summers of 1990 and 1991 (Oerlemans and Vugts, 1993). This study analyzes the satellite TB data along the 67°N parallel from −50°E to −43°E. Fig. 1 (a) shows the transect overlaid on the digital elevation model of the Greenland Ice Sheet (Howat et al., 2014). Surface mass balance and ice velocity measurements have been performed at nine locations along the K-transect, four of which are equipped with AWS measurement sites: two in the ablation zone (annual net loss of mass) at approximately 350 m and 670 m above sea level (ASL), one at the approximate equilibrium-line altitude (~1270 m ASL), and one in the lower accumulation zone (annual net gain of mass) (~1840 m ASL) at distances of 5, 38, 88, and 140 km from the ice edge, respectively. We used the air temperature measurements from these four AWS sites (Table 1). Fig. 1 (b) shows the transect's elevation profile with the stations' locations.

3. Approach

3.1. Brightness temperature response to melt

To analyze the SMAP and AMSR2 observations along the focus transect, the TB measurements were extracted from the grid pixels closest to the latitudinal parallel at 67°N. The in situ AWS sites provide local measurements of the near-surface air temperature at four points along the regional transect and its evolution over time, while the TB measurements have a continuous coverage along the transect (at about 9 km intervals). We investigated the correspondence of the change of the different TB channels (from the fully frozen winter reference values) with respect to the thermal evolution established by the AWS air

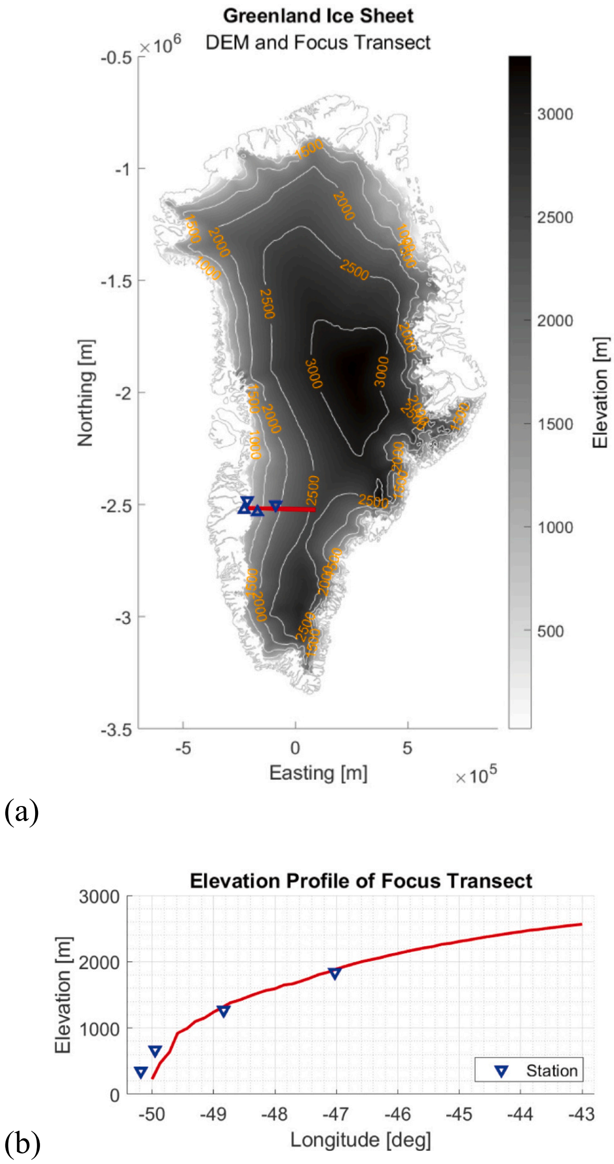

Fig. 1. (a) The digital elevation model (DEM) of the Greenland Ice Sheet (Howat et al., 2014) and the focus transect with the station locations. The map is plotted in polar stereographic coordinates (Snyder, 1987). (b) The elevation profile along the focus transect based on (Howat et al., 2014) and the locations of the stations (the westernmost station is just outside of the ice sheet) with their recorded elevations.

Table 1
K-transect automatic weather stations (AWS) used in this study.

Station Name	Latitude (°N)	Longitude (°W)	Elevation [m] (Above Sea Level)
KAN_B	67.1252	50.1832	350
KAN_L	67.0955	49.9513	670
KAN_M	67.0670	48.8355	1270
KAN_U	67.0003	47.0253	1840

temperature measurements. The winter reference values were computed using the measurements just before the start of the melt season from April 1 to April 6.

3.2. Approach for retrieving the profile of snow status (wet/dry)

We investigated the difference between the 1.4 GHz to 36.5 GHz melt indications to identify temporal and spatial trends of subsurface meltwater evolution. As was shown in Colliander et al. (2022), all frequency bands in the 1.4–36.5 GHz range respond clearly to the seasonal melt events on the ice sheet. The snow status (wet/dry) was compared to identify cases when the lower frequencies indicate melt conditions (wet state), but the higher frequencies show frozen conditions (dry state). In these cases, the lowest frozen channel indicates the thickness of the frozen layer and how deep the seasonal meltwater has percolated within the firn. Identifying these cases is particularly important for understanding the melt processes affecting the ice sheets.

We used a saturation fraction (SF) similar to what was used in Colliander et al. (2022) to determine whether the emissions were affected by meltwater with respect to winter conditions. We chose a uniform approach across frequencies for consistency, although there are melt detection approaches explicitly developed for Ka-band (such as Tedesco, 2009) and L-band (such as Mousavi et al., 2022). These approaches are also based on the change of the TB values from winter reference conditions, with some refinements. SF is defined here as:

$$SF_p(f) = \frac{T_{B,p}(f) - T_{B,p}^{frozen}(f)}{T_{B,p}^{max}(f) - T_{B,p}^{frozen}(f)} \tag{1}$$

where $SF_p(f)$ is the frequency-dependent saturation fraction and $T_{B,p}(f)$ represents TB with the subscript p indicating the polarization; $T_{B,p}^{frozen}(f)$ and $T_{B,p}^{max}(f)$ represent TB during reference fully frozen winter conditions and the maximum TB during the melt season, respectively. Cases having saturation fractions less than zero from (1) are reported as saturation fraction zero. The period used to compute the winter reference value was January and December of each water year, before and after the melt season. The threshold for detecting binary snow/firn status (wet/dry) was set as Z times the average standard deviation of the winter reference. The smaller the value of Z, the more sensitive the detection is to deviations from the reference value, but also more prone to false indications of melt. Conversely, the larger the value, the less sensitive the detection is to deviations from the winter reference value but also less prone to making false melt indications (Mousavi et al., 2022). A value of $Z = 6$ generally gave a balanced response to SF variations for all frequencies.

The melt detected with different frequencies was assigned to five layers so that the 36.5 GHz channel corresponded to the first layer and the 1.4 GHz channel to the last layer. We did not attempt to characterize the depths and thicknesses of the layers, but their order is unequivocal and serves the study's objective to explore the meltwater response of the different frequencies in the surface and subsurface layers of ice sheets. Conversely, to assign an estimate at which depths these snow status (dry/wet) changes occur would require an additional modeling step. To compute the emission propagation at different frequencies, information on parameters such as snow density, temperature, and grain size would be needed, in addition to the snow status information, for all pixels. Each channel has its characteristic sensing depth in snow depending on these parameters, varying from tens of centimeters for 36.5 GHz to hundreds of meters for 1.4 GHz. Estimation of the depth profiles of these parameters is not a trivial task, especially at the pan-Greenland scale; particularly, the variable and largely unknown extent of structures like ice pipes and lenses significantly complicate the depth calculation. Making these estimates is the next obvious step in exploring multi-frequency retrieval, but it is outside the scope of the presented work.

To spatially visualize the vertical distribution of snow status, the different melt scenarios were color coded. Fig. 2 shows the different scenarios. The cases vary from only the first layer in wet snow status (Scenario 1) to all layers potentially in wet snow status (Scenario 5) to only the last layer in wet snow status (Scenario 11). To keep the number

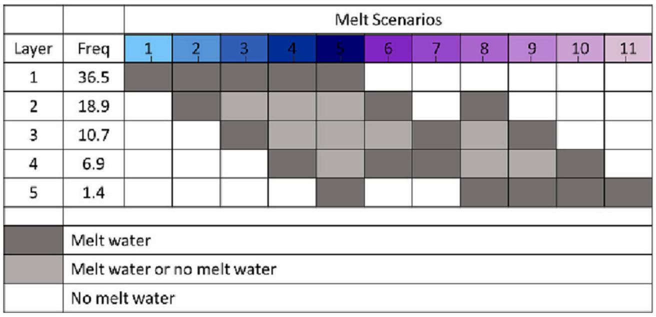

Layer	Freq	Melt Scenarios										
		1	2	3	4	5	6	7	8	9	10	11
1	36.5	■	■	■	■	■	□	□	□	□	□	□
2	18.9	□	■	▒	▒	▒	■	□	■	□	□	□
3	10.7	□	□	■	▒	▒	▒	■	▒	■	□	□
4	6.9	□	□	□	■	▒	■	■	▒	▒	■	□
5	1.4	□	□	□	□	■	□	□	■	■	■	■

■	Melt water
▒	Melt water or no melt water
□	No melt water

Fig. 2. Meltwater profile classification for up to five snow layers of relative, undefined depths ranging from the surface layer (1) to the deepest layer (5). Each row represents a different layer associated with a frequency (GHz) identified in the left columns, while the rest represent the different melt scenarios. The color coding is used in Fig. 7.

of cases reasonable but at the same time informative, in scenarios involving multiple layers, the layers between the highest and lowest are allowed to be either in a wet or dry state. For example, in case 3, Layers 1 and 3 are wet, while Layer 2 may be wet or dry. The snow status profile was also analyzed along the focus transect. The status of each layer was plotted with the saturation factor (SF) and its thresholds along the transect.

3.3. Computation of seasonal melt and refreeze timing differences

The daily AM and PM overpass melt indications at each frequency were calculated to analyze the overall differences in the meltwater presence detected by each frequency. The number of days when the first layer was frozen, but the deeper layers still had meltwater, was compared to the number of days when at least the first layer was frozen. This shows the significance of accounting for the lower frequencies for tracking the ice sheet melt evolution. Similarly, the last day of melt detected at each frequency was compared to other frequencies to analyze the differences in the refreeze timing.

4. Results

4.1. Brightness temperature response to snow status (wet/dry) profile

Fig. 3 shows the TB measurements at 1.4, 6.9, 10.7, 18.9 and 36.5 GHz along the focus transect (Section 2.3) averaged over April 1–6, 2019, which represents winter conditions just before the start of the melt season. The variation from the low-elevation edge of the ice sheet toward the high-elevation interior decreases systematically with frequency for both polarizations. The values are higher in the ablation zone, decrease rapidly over the percolation zone, and increase again approaching the dry snow line. The variation is likely caused by differences in the internal structure of the ice sheet in these different zones affecting the lower frequency measurements that see emissions originating from deeper in the ice sheet than the higher frequencies (e.g., Jezek et al., 2018). Fig. 4 shows a similar TB trend from the ice sheet's edges toward the interior over much of Greenland.

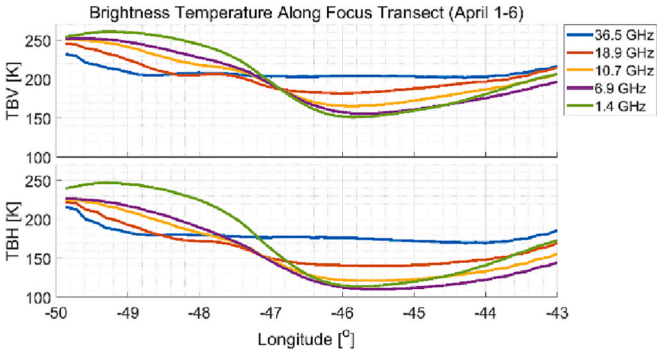

Fig. 3. V and H polarized brightness temperatures for 1.4, 6.9, 10.7, 18.9, and 36.5 GHz along the focus transect (Section 2.3) averaged for April 1–6, 2019.

Fig. 5 shows the difference between the V and H polarized TB measurements with respect to the winter reference values at 1.4 to 36.5 GHz along the focus transect (Section 2.3) for seven days during the 2019 melt season. The plots show the evolution of the TB difference from a frozen condition on April 25, 2019 (A) to a refrozen condition on September 25, 2019 (G). The plots indicate the AWS temperatures with bars whose locations correspond to stations along the transect. At step B (May 28), the melt is starting from the west (lower elevation, see Fig. 1 (b)) as indicated by air temperature measurements from stations KAN_B, KAN_L, and KAN_M. At steps C and D (June 9 and August 8), the melt spreads further east to higher elevations. At step E (August 10), the refreeze starts and the easternmost station (KAN_U) indicates below-freezing temperatures. Step F (August 17) indicates the progression of refreeze, while the AWS temperatures are similar to step E. Step G represents the refrozen condition, as KAN_L, KAN_M, and KAN_U are below freezing, although KAN_B at the edge of the ice sheet is slightly above freezing.

The TB measurements in Fig. 5 correspond to melt and refreeze trends indicated by the AWS measurements. Here a positive ΔTBV or ΔTBH (referred to as ΔTB here for brevity because they are very consistent) for 6.9 to 36.5 GHz and any deviation of ΔTB from zero for 1.4 GHz is considered an indication of melt conditions. Starting with Step B, the ΔTB for all frequencies deviates from zero starting from the west to about halfway between KAN_M and KAN_U (correspondingly, KAN_M is above freezing and KAN_U is below freezing), which corresponds to melt progressing up to this point. At step C, ΔTB deviation extends up to KAN_U for all frequencies except for 1.4 GHz (KAN_U is changed to above freezing), corresponding to melt now extending up this point. The fact that the 1.4 GHz channel is still close to zero is likely due to the insensitivity of the long wavelengths to small meltwater amounts. At Step D, the 1.4 GHz ΔTB is non-zero at KAN_U along with the other frequencies, and the deviation extends up to about −44° longitude, suggesting further spreading of melt up to this point. At step E, the 36.5 GHz ΔTB drops below zero on the transect's eastern side, indicating refreezing (and corresponds to KAN_U changing to below freezing). The positive deviation of ΔTB at the lower frequencies east of KAN_U suggests that there is still meltwater in the deeper layers. At step F, 36.5 GHz and 18.9 GHz ΔTB are close to or below zero further west but are still above zero west from KAN_M (which is above freezing). Also, the ΔTB deviation for the lower frequencies is smaller and now extends only up to about −45° longitude, indicating the progress of refreezing of the subsurface layers toward the west. Finally, at step G the refreeze is complete. The 1.4, 6.9, and 10.7 GHz ΔTB return very close to zero (their winter reference values), but the 18.9 and 36.5 GHz channels exhibit variable deviation from the winter reference along the transect, which is likely due to the effect of snow morphology in the surface layers during the melt season altering the TB for the frozen conditions. The lower frequencies are less sensitive to these changes. The V and H polarized signatures are generally similar. The results indicate that the spatio-temporal response of the multifrequency TB measurements to snow status (wet/dry) changes consistent with what Colliander et al. (2022) observed over a single site.

Notably, the 1.4 GHz TB change behaves differently between the ablation and percolation zones, while the other frequencies show a similar response over the two zones, which was also reported by Mousavi et al. (2021). Over the ablation zone and approaching the dry snow line, the TB during melt becomes smaller than the winter reference, a deviation of the response from the other frequencies. Over the percolation zone, the TB becomes larger during the melt. Increased TB during melt is generally explained by increased emission when liquid

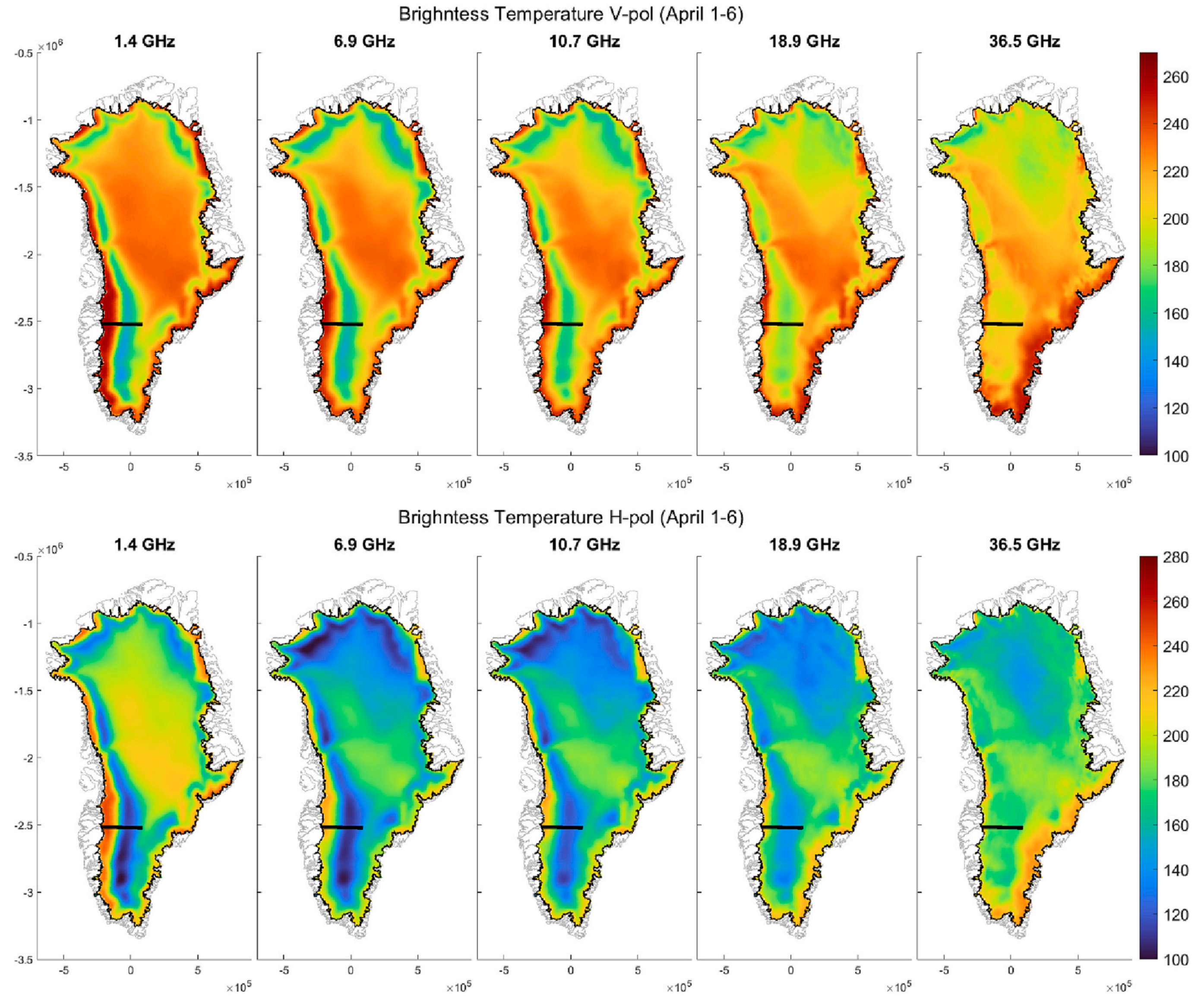

Fig. 4. V and H polarized brightness temperatures (K) for 1.4, 6.9, 10.7, 18.9, and 36.5 GHz averaged for April 1–6, 2019. The focus transect. (Section 2.3) is marked with a black line. The maps are plotted in polar stereographic coordinates (Snyder, 1987).

water is present in the snow and firn (e.g., Mote and Anderson, 1995). The ablation zone is characterized by higher TB for the lower frequencies during winter conditions, with the 1.4 GHz channel having the highest TB level (Fig. 3 and Fig. 4). The effects of meltwater in the snow and firn reduce the emission for 1.4 GHz in this case but not for the other frequencies. The reason for this is likely the smaller absorptive effect of the meltwater at 1.4 GHz compared to the higher frequencies, combined with the higher background emission emanating from the deeper layers that are not visible to the higher frequencies.

4.2. Snow status (wet/dry) profile retrieval results

Fig. 6 shows the meltwater retrieval for the focus transect (Section 2.3) using the approach explained in Section 3.2. The top panels of the plots show the saturation factor (SF) along the transect for each frequency and the associated threshold, and the bottom panel shows the snow status (wet/dry) projected to different layers based on the frequency. The blue coloring indicates melting. The left-hand column shows the snow status (wet/dry) for the same PM overpasses as Fig. 5, and the right-hand column shows the snow status (wet/dry) for the overpass immediately after the first one. These are AM overpasses, and the differences between the left and right plots demonstrate the diurnal cycle of the melt-refreeze dynamics. The plots are generated using the V polarized TB – the result is very similar to the H polarized TB based on Section 4.1.

The plots show the different levels of threshold values for each frequency. Generally, the higher frequencies have higher thresholds because of their higher TB variance during the winter reference period (the variances were 1.6, 2.6, 3.3, 4.9, and 8.4 K for the V polarization from lowest to highest frequency). This is caused by the increased propagation effects of the shorter wavelengths to temporal variations in surface temperature and structural changes in the surface snow. The bottom panels illustrate the evolution of the melt during the melt-refreeze cycle in different layers. Over the season, the melt front progresses toward the east, and meltwater persists in deeper layers, while the surface layer typically refreezes during the AM overpasses. Later in the season, the surface refreezes first, and then the deeper meltwater refreezes, progressing toward the west.

Between the ablation and accumulation zones, there is a region with a minimal difference between the frozen condition and melt-affected TB at 1.4 GHz, which makes detecting melt difficult and may introduce artifacts in the melt retrieval. In this zone, the TB remains relatively

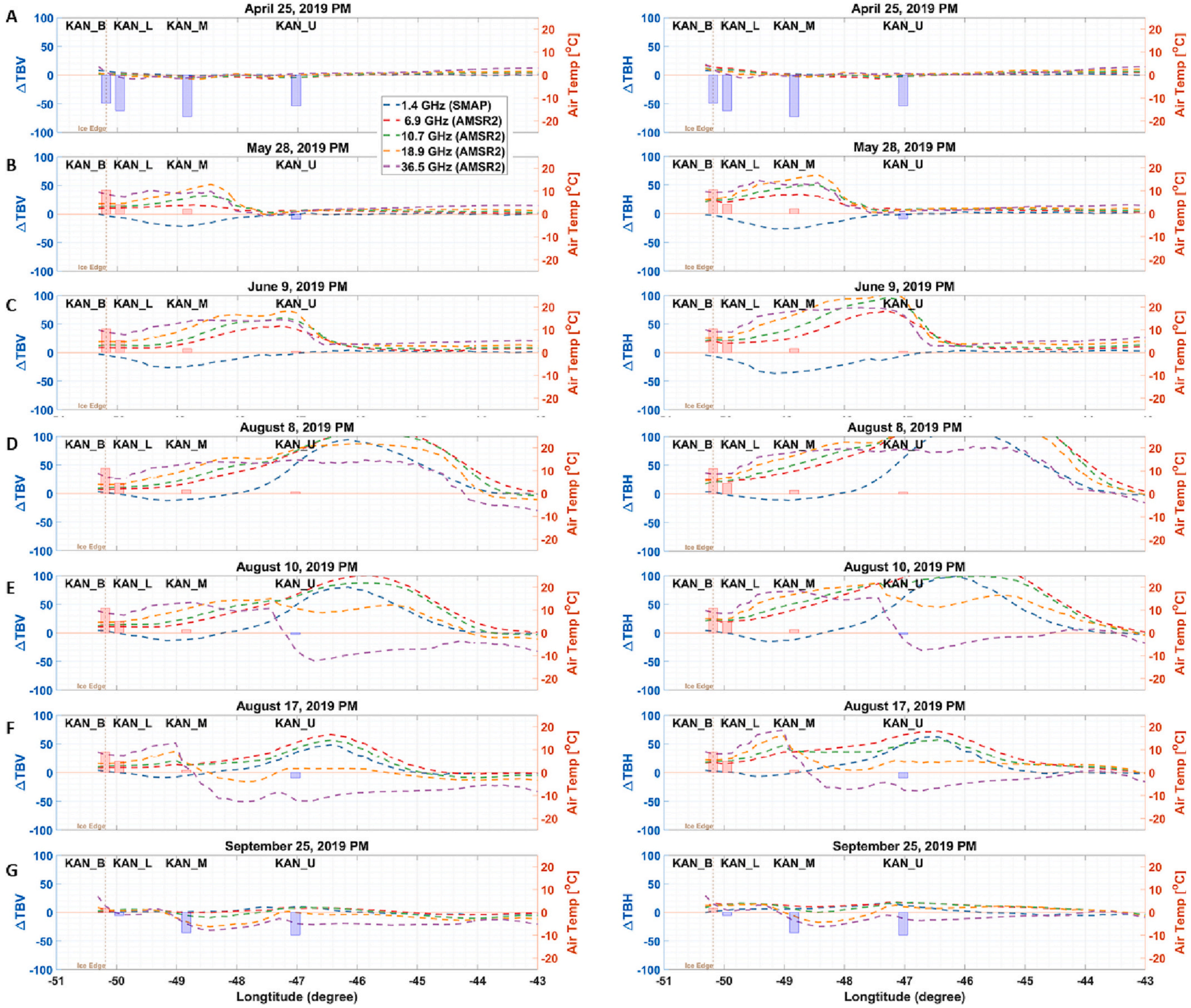

Fig. 5. V (left-hand side column) and H (right-hand side column) polarized 1.4 GHz to 36.5 GHz brightness temperature (TB) change with respect to the winter reference values (in K) for the east-west focus transect (Section 2.3) and air temperature measurements (in °C) indicated with vertical bars for four automatic weather stations at their respective locations along the transect during the 2019 melt season. The plots show the PM overpass TB evolution from a frozen state on April 25, 2019 (A) to a refrozen state on September 25, 2019 (G).

stable regardless of snow status (see also Fig. 5). The effect is particularly notable in the PM plots (D, E, F) in Fig. 6, where there is a "hole" in the bottom layer melting around −48° longitude.

Fig. 7 shows the snow status profile using the classification described in Section 3.2 for the entire Greenland Ice Sheet for the exact dates as in Fig. 5 and Fig. 6. The evolution of the melt and refreeze cycle across Greenland follows a similar pattern as along the focus transect. Early in the season, the melt spreads toward the higher elevation interior, experiencing diurnal refreeze cycles on the surface and persistent melt deeper within the firn. Later in the season, the refreeze starts from the surface and interior and spreads toward the lower elevation edges, with the surface remaining largely frozen. On September 25, 2019 (G), the transect was almost entirely frozen, although some meltwater was still slowly refreezing in eastern Greenland. By October 31, 2019 (H), most of the melt is refrozen, and there are only some residual indications of deep subsurface meltwater in the southeastern edge of the ice sheet, which correspond to contributions of depth-integrated emissions from perennial firn aquifers, locations of which were mapped in Miller et al. (2020) using 1.4 GHz TB.

4.3. *Seasonal melt and refreeze timing differences between frequencies*

Fig. 8 shows maps for the number of melt days for AM and PM overpasses at 1.4 GHz, 6.9 GHz, and 36.5 GHz V polarization for 2016–2019. There are significant differences between the frequencies, which remain relatively consistent from year to year. The difference between AM and PM is relatively small for the 1.4 and 6.9 GHz observations but more substantial for the 36.5 GHz observations. The number of melt days at the 1.4 GHz and 36.5 GHz channels are generally lower than for the 6.9 GHz channel, but likely for different reasons. The 1.4 GHz observations are less sensitive to small meltwater amounts, to which 36.5 GHz observations are particularly sensitive (Colliander et al., 2022). The 6.9 GHz channel is affected by persistent subsurface meltwater, even in smaller amounts. However, as our results showed, the 36.5 GHz observations are more sensitive to the surface refreeze throughout the melt season than the lower frequencies, reducing the

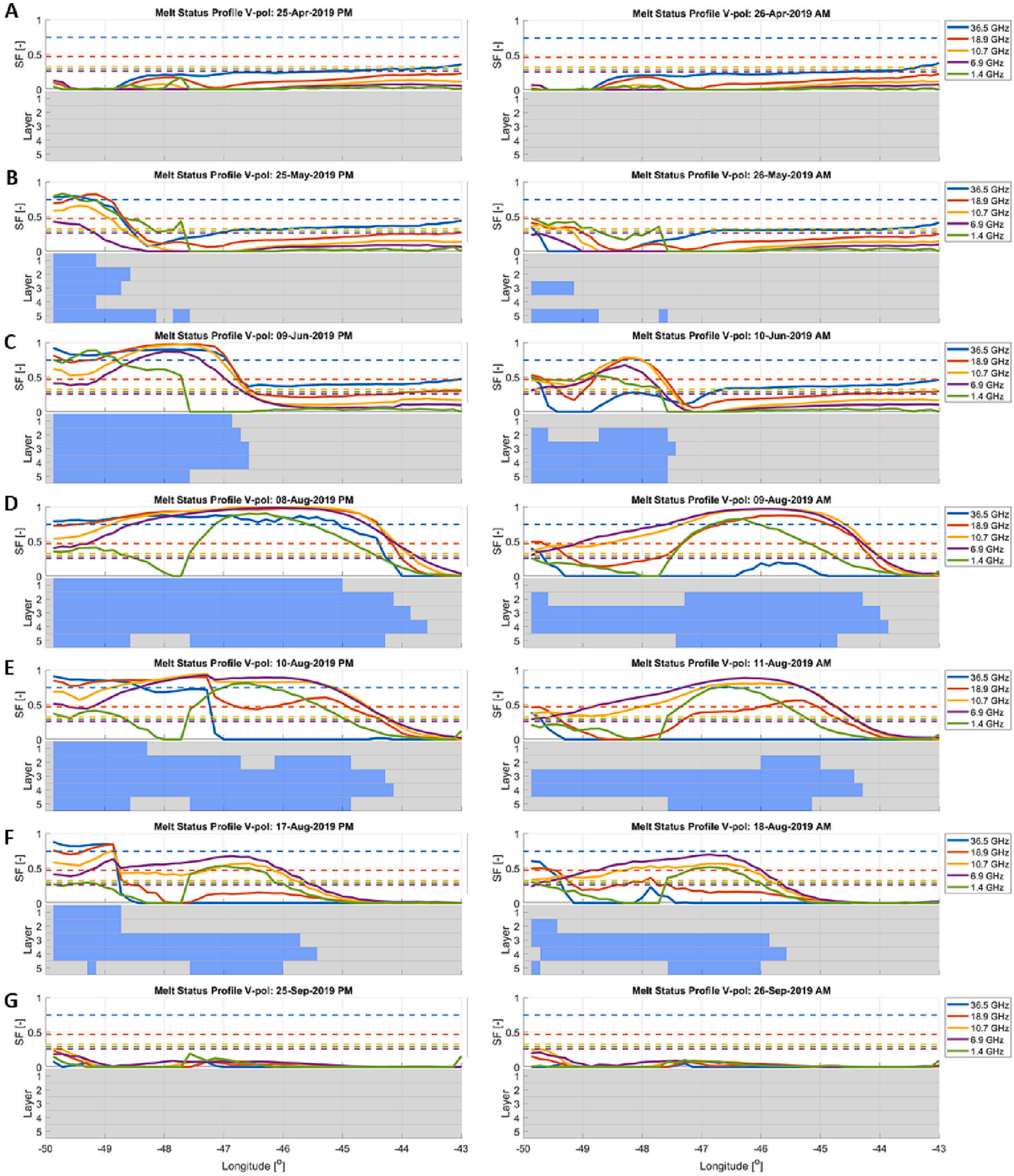

Fig. 6. Snow status (wet/dry) retrieval along the focus transect (Section 2.3). The top panel of each plot shows the saturation factor (SF) and its thresholds (dashed lines) for each TB frequency channel; the bottom panel shows the snow status projected to each layer based on the frequency (the layers are populated top-down with the snow status derived from 36.5 GHz to 1.4 GHz channels). The blue color indicates melt. The left-hand column shows the results for the same (PM) overpasses as Fig. 5, and the right-hand side shows the results for the next (AM) overpass. (For interpretation of the references to color in this figure legend, the reader is referred to the web version of this article.)

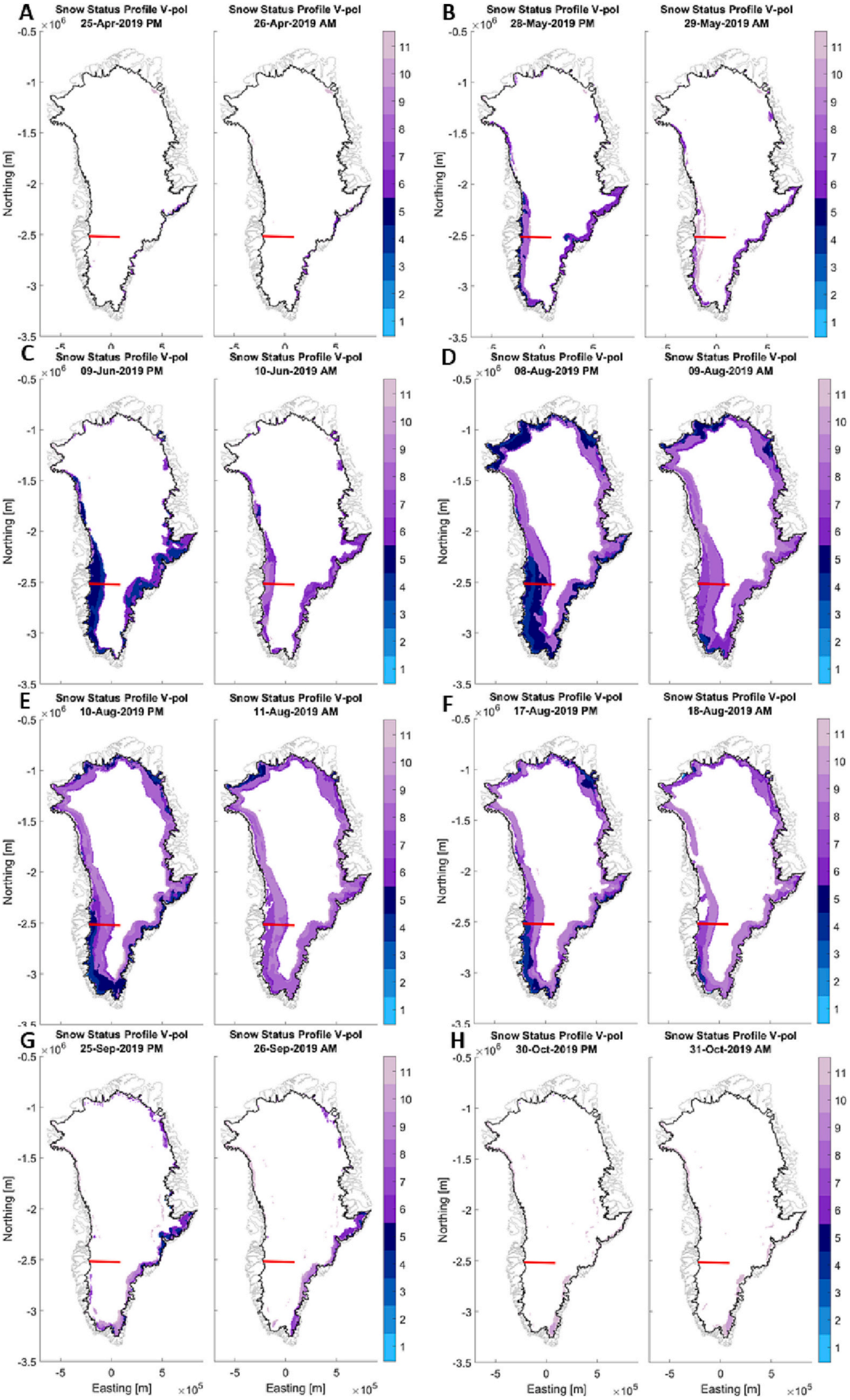

Fig. 7. Maps of the melt profile for the exact dates as in Fig. 5 and Fig. 6. The left panel of each image pair shows the PM overpass, and the right panel shows the AM overpass. The focus transect (Section 2.3) is highlighted with a red line. The color coding is explained in Fig. 2. The maps are plotted in polar stereographic coordinates (Snyder, 1987). (For interpretation of the references to color in this figure legend, the reader is referred to the web version of this article.)

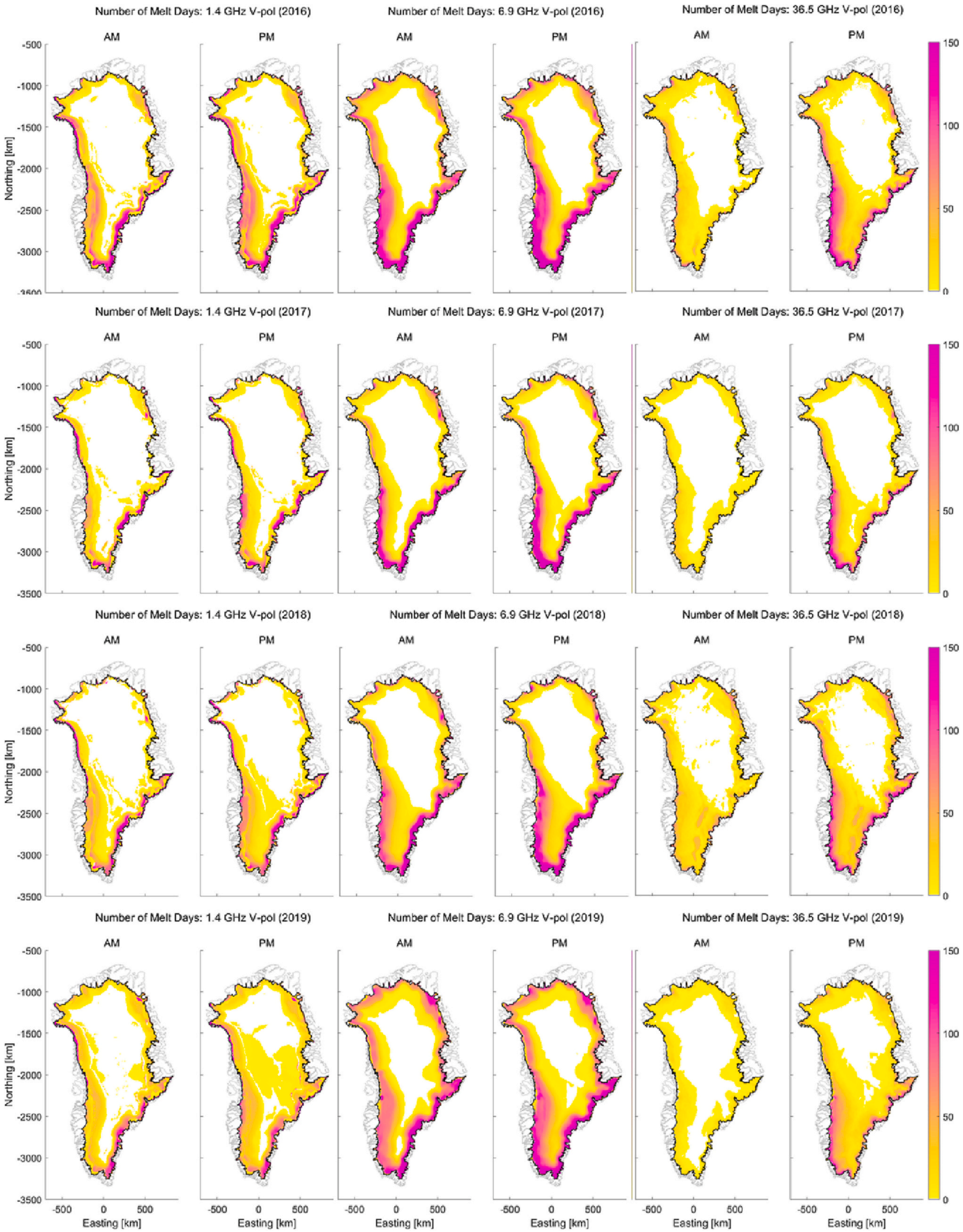

Fig. 8. Number of melt days for AM and PM overpasses at 1.4 GHz, 6.9 GHz, and 36.5 GHz for 2016–2019. The maps are plotted in polar stereographic coordinates (Snyder, 1987).

number of overall frozen days. This is also the reason for the substantial difference between AM and PM results. The persistent meltwater in deeper layers indicated from the lower frequency observations is less impacted by diurnal refreeze cycles relative to the higher frequency observations that are primarily sensitive to surface conditions. Both 6.9 GHz and 1.4 GHz retrievals show a smaller extent of sporadic melt events occurring toward the colder northern interior of Greenland than the 36.5 GHz retrievals. The 1.4 GHz retrievals are also affected by spatial differences in ice sheet structure between the ablation and percolation zones. The 2019 result for the 1.4 GHz observations is affected by the SMAP outage from June 20 to July 22.

Fig. 9 illustrates the number of days when the 36.5 GHz band indicated the surface was frozen in contrast with meltwater persistence within the ice sheet indicated by the 6.9 GHz band. The 1:30 AM overpasses observe this consistently during diurnal surface refreeze cycles throughout the melt season. The 1:30 PM overpasses observe this condition on fewer days than the AM overpasses because the surface melt is more common during the afternoon hours; the condition of a frozen surface with meltwater deeper in the layers occurs only during the refreeze after more significant melt events.

The results suggest that the high-frequency retrievals do not capture the spatially and temporally significant subsurface meltwater refreeze processes.

Fig. 10 shows the refreeze timing for 2016–2019 at each frequency. The largest difference is between the 6.9 GHz and 36.5 GHz channels for each year except 2017. In 2017, a multi-day melt anomaly in late October affected all frequencies (verified with the focus transect AWS temperature measurements). As mentioned above, the 36.5 GHz observations indicate the refreeze of the surface layer and are not sensitive to the presence of meltwater in the deeper layers, as are the 6.9 GHz observations. Two factors are expected to affect the difference between the 1.4 GHz and 6.9 GHz measurements. First, the 1.4 GHz observations are less sensitive to small surface melt events than the 6.9 GHz measurements. The 1.4 GHz observations are also less sensitive to small residual melt amounts that may be found in the subsurface. Fig. 11 shows the differences in refreeze timing between 1.4 GHz and 36.5 GHz melt detections and 6.9 GHz and 36.5 GHz melt detections. There are some substantial areas where it seems the 36.5 GHz channel detected melt later than the 1.4 GHz channel, which may be driven by the higher sensitivity of 36.5 GHz to small melt events and/or the earlier PM overpass time of AMSR2, which may be more conducive to capturing the warmest conditions of the day. Conversely, there are few areas where the 36.5 GHz TB detected melt events later than the 6.9 GHz TB observation, which is likely because the 6.9 GHz channel remains sensitive to small surface events compared to the 1.4 GHz channel (Colliander et al., 2022); although there is also an overpass timing difference between 1.4 GHz and the other frequencies (see Sections 2.1 and 2.2).

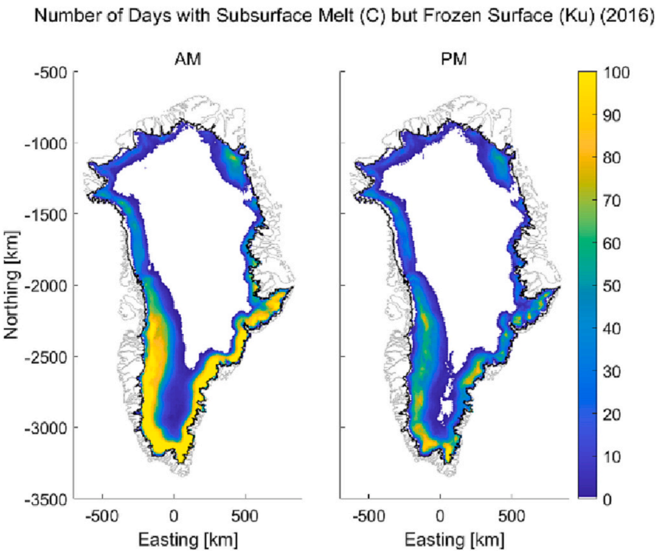

Fig. 9. Number of days when the surface was frozen based on the 36.5 GHz channel, but where there was still meltwater within the ice sheet based on the 6.9 GHz channel. The maps are plotted in polar stereographic coordinates (Snyder, 1987).

5. Discussion

First, the results suggest that melt detected from lower frequency (1.4, 6.9, and 10.7 GHz) passive microwave observations is robustly linked to meltwater presence deeper in the snow/firn/ice continuum than the surface conditions represented from higher frequency (Ku- and Ka-band) measurements. These results are based on TB comparisons with surface air temperature measurements from AWS stations distributed along a Greenland environmental transect and are also consistent with the single location-based conclusion of Colliander et al. (2022). The current study extended the multifrequency TB and melt assessment over the pan-Greenland domain. Second, the differences between surface and subsurface melt-refreeze cycles show large spatial and temporal diversity, resulting from different climate conditions and ice sheet stratigraphy in different ice sheet regions. These differences manifest in both the number of melt days during the melt season, and the timing of seasonal refreeze, notably in perennial firn aquifer areas in southeastern and southern Greenland.

There are two important aspects regarding how the lower frequency measurements add value to satellite detections. While melt onset at all frequencies tends to behave relatively uniformly as a result of the sensitivity to the emergence of meltwater in the near-surface layers, surface and subsurface refreezing reveal new insight regarding climate- and stratigraphy-induced ice sheet melt dynamics absent from traditional higher-frequency melt detection algorithms. The lower frequencies are also sensitive to larger meltwater amounts, whereas the highest frequencies convey mainly a binary condition of the shallow near-surface snow status (wet/dry). Therefore, a natural next step is a quantified meltwater profile retrieval. Mousavi et al. (2021, 2022) demonstrated a total LWC retrieval algorithm using single frequency (L-band) TB data. Incorporating complementary information from higher frequencies holds the potential for delineating liquid water content profiles. This prospect is further supported by the relative consistency in the frequency-dependent response across the entire Greenland ice sheet. However, in developing such algorithms, the various geographic and climate regimes across the ice sheet can nevertheless manifest additional uncertainties, especially the differences between the ablation and percolation zones and their boundaries. Also, perennial firn aquifer regions will require more investigation, as wet firn deep in the ice sheet can affect the 1.4 GHz observations (Miller et al., 2020). In principle, the change detection approach is less sensitive to these effects because spatial changes in the TB level are accounted for using spatially varying reference conditions. However, more sophisticated modeling of the emission from the entire ice sheet column may be needed to account for both the potentially large amounts of liquid water deep in the firn and in layers closer to the surface.

We acknowledge two limitations in the presented study. First, the melt detection algorithm used in this study is very simple and consistent across frequencies, which may introduce uncertainties. However, as shown from prior studies (e.g., Colosio et al., 2021), different melt detection algorithms developed for a single frequency can lead to different results. Therefore, picking a previously developed algorithm for 36.5 GHz would not necessarily represent more accurate results for that frequency. The fundamental problem is the lack of validation data that could be used to assess the accuracy of the algorithms in a robust way, which is related to the second limitation of the presented study. Even though the focus transect AWS air temperature-based validation demonstrates a high consistency in the frequency-dependent response,

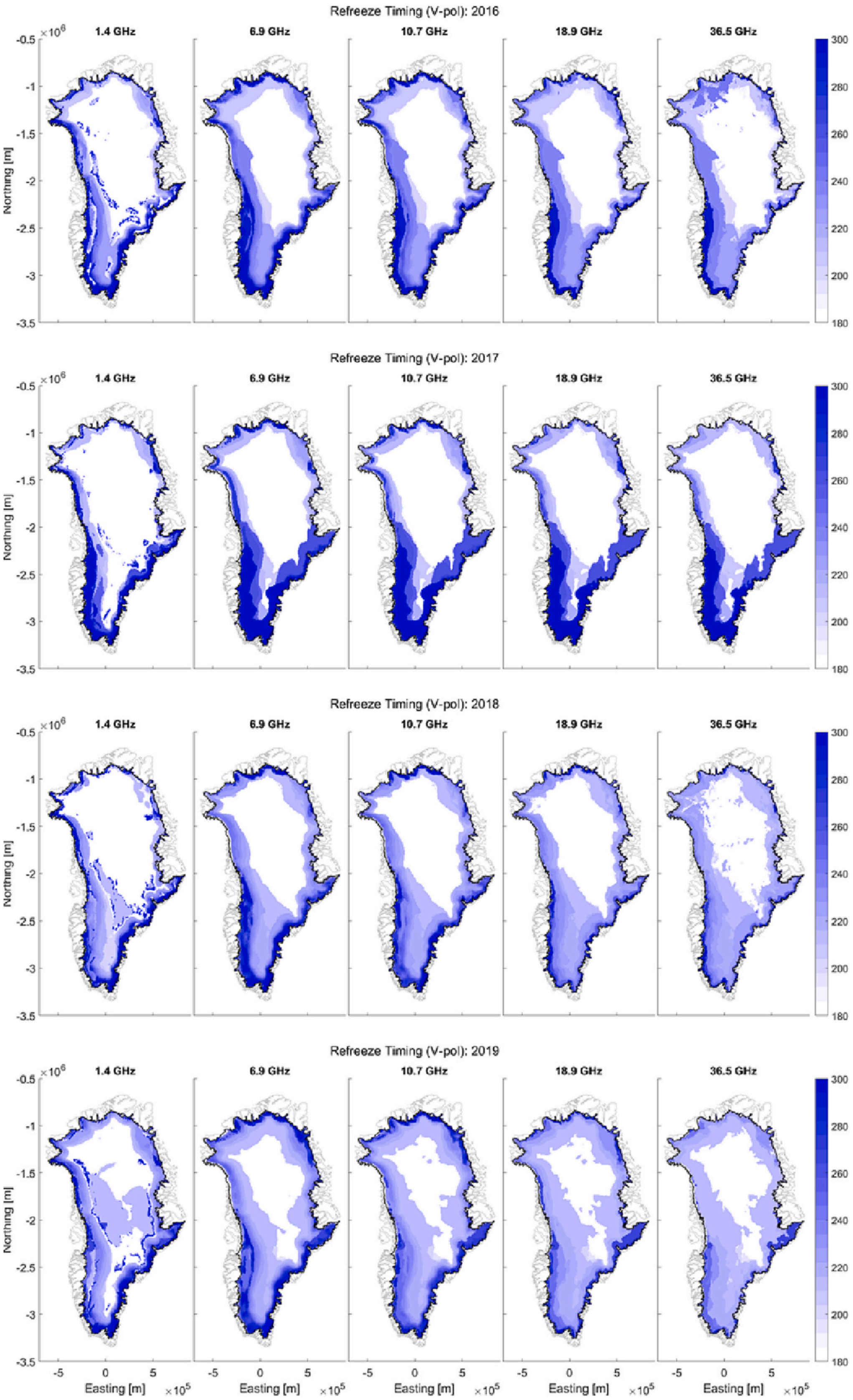

Fig. 10. Refreeze timing in the day of the year for 2016–2019 based on melt detections from the different TB frequency channels. The maps are plotted in polar stereographic coordinates (Snyder, 1987).

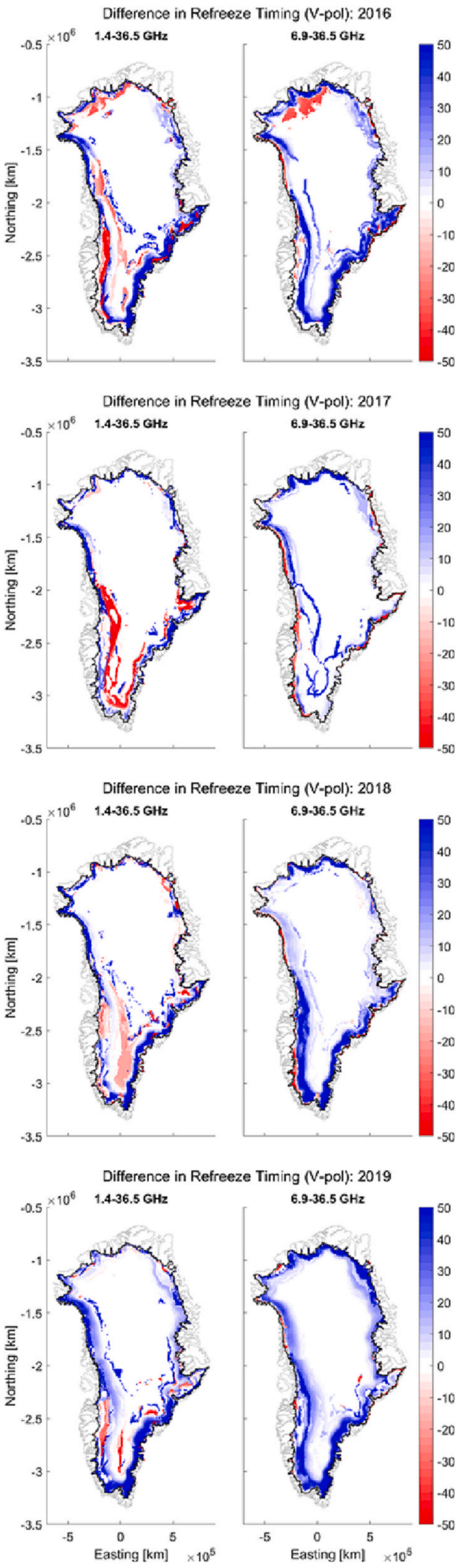

Fig. 11. Refreeze timing differences (in days) between 1.4 GHz and 36.5 GHz melt detections and 6.9 GHz and 36.5 GHz melt detections. Blue means the lower frequency had a later last melt day, and the red color means that the 36.5 GHz channel had a later last melt day. The maps are plotted in polar stereographic coordinates (Snyder, 1987). (For interpretation of the references to color in this figure legend, the reader is referred to the web version of this article.)

the validation is limited to only four station locations, and the analysis does not include subsurface measurements. There are more air temperature measurements available over the Greenland ice sheet. Still, as they do not represent actual melt conditions, the spatially and temporally consistent evidence provided by the focus transect captures the most critical aspects of the melt-refreeze dynamics addressed in this study.

6. Conclusion

This study represents a first step in understanding the spatiotemporal multifrequency TB response to seasonal melt over the entire Greenland ice sheet. The results show a consistent frequency-dependent response to melt-refreeze events across the ice sheet. The unique melt indications derived at different frequencies showed persistent seasonal subsurface meltwater and delayed subsurface refreezing of the seasonal meltwater. The result indicates widespread seasonal subsurface persistent meltwater occurrences missing from the high-frequency retrievals commonly used for satellite monitoring Greenland ice sheet melt dynamics. Additional complementary lower frequency (1.4 GHz, 6.9 GHz, and 10.7 GHz) TB observations are necessary to fully capture the variable melt-refreeze cycles and meltwater distribution in different ice layers. These results provide the basis for developing more comprehensive algorithms and retrievals of meltwater profiles driven by overlapping multifrequency TB observations from SMAP, SMOS, AMSR2, and other operational satellite radiometers. The next generation ESA-EU Copernicus Imaging Microwave Radiometer (CIMR) will provide simultaneous multi-frequency (L-band to Ka-band) TB measurements from a single platform and nested sampling footprint, offering enhanced capability and performance for monitoring ice sheet melt dynamics.

CRediT authorship contribution statement

Andreas Colliander: Conceptualization, Methodology, Software, Formal analysis, Writing – original draft, Funding acquisition. **Mohammad Mousavi:** Software. **John S. Kimball:** Writing – review & editing, Funding acquisition. **Julie Z. Miller:** Writing – review & editing. **Mariko Burgin:** Software.

Declaration of Competing Interest

The authors declare that they have no known competing financial interests or personal relationships that could have appeared to influence the work reported in this paper.

Data availability

The SMAP L1CTBE brightness temperature data is available through National Snow and Ice Data Center (NSIDC): https://doi.org/10.5067/XB8K63YM4U8O). The AMSR2 data is available through the JAXA data service: https://gportal.jaxa.jp/gpr/. The focus transect AWS data is available here: https://doi.org/10.22008/FK2/8SS7EW (Fausto et al., 2021). The layered snow status (dry/wet) maps are posted at Colliander (2023), and the codes used to generate the data are available at: https://github.com/acjpl/greenland_snow_status_profile_RSE23.

Acknowledgment

This work was performed at thte Jet Propulsion Laboratory, California Institute of Technology, under a contract with the National Aeronautics and Space Administration (80NSSC18K0980 & 80NM0018F0585). The Greenland maps were generated with the assistance of the Arctic Mapping Tools (Greene et al., 2017).

References

Abdalati, W., Steffen, K., 1995. Passive microwave-derived snow melt regions on the Greenland ice sheet. Geophys. Res. Lett. 22 (7), 787–790.

Brodzik, M.J., Billingsley, B., Haran, T., Raup, B., 2012. EASE-Grid 2.0: Incremental but Significant Improvements for Earth-Gridded Data Sets. ISPRS Int. J. Geo-Inf. 1 (1), 32–45. https://doi.org/10.3390/ijgi1010032.

Brodzik, M.J., Billingsley, B., Haran, T., Raup, B., Savoie, M.H., 2014. EASE-Grid 2.0: Incremental but Significant Improvements for Earth-Gridded Data Sets. ISPRS International Journal of Geo-Information 3 (3), 1154–1156. https://doi.org/10.3390/ijgi3031154.

Chaubell, J., Chan, S., Dunbar, R.S., Peng, J., Yueh, S., 2020. SMAP Enhanced L1C Radiometer Half-Orbit 9 km EASE-Grid Brightness Temperatures, Version 3. NASA National Snow and Ice Data Center Distributed Active Archive Center, Boulder, Colorado USA. https://doi.org/10.5067/XB8K63YM4U8O.

Colliander, A., Mousavi, M., Marshall, S., Samimi, S., Kimball, J.S., Miller, J., Johnson, J., Burgin, M., 2022. Ice sheet surface and subsurface melt water discrimination using multi-frequency microwave radiometry. Geophys. Res. Lett. Vol. 49, Issue 4 https://doi.org/10.1029/2021gl096599.

Colliander, Andreas, 2023. Greenland snow status profile. Mendeley Data V1. https://doi.org/10.17632/b5n4k9zkrk.1.

Colosio, P., Tedesco, M., Ranzi, R., Fettweis, X., 2021. Surface melting over the Greenland ice sheet derived from enhanced resolution passive microwave brightness temperatures (1979–2019). Cryosphere 15, 2623–2646. https://doi.org/10.5194/tc-15-2623-2021.

Cox, C., Humphrey, N., Harper, J., 2015. Quantifying meltwater refreezing along a transect of sites on the Greenland ice sheet. Cryosphere Vol. 9(2, 691–701. https://doi.org/10.5194/tc-9-691-2015.

Entekhabi, D., Kellogg, K., O'Neill, P., Yueh, S., 2014. SMAP Handbook – Soil Moisture Active Passive: Mapping Soil Moisture and Freeze/Thaw from Space. SMAP Project. Jet Propulsion Laboratory, Pasadena, CA.

Entekhabi, D., Njoku, E.G., O'Neill, P.E., Kellogg, K.H., Crow, W.T., Edelstein, W.N., Entin, J.K., Goodman, S.D., Jackson, T.J., Johnson, J., Kimball, J., Piepmeier, J.R., Koster, R.D., Martin, N., McDonald, K.C., Moghaddam, M., Moran, S., Reichle, R., Shi, J.C., Van Zyl, J., 2010. The Soil Moisture Active Passive (SMAP) Mission. Proceedings of the IEEE 98 (5), 704–716. https://doi.org/10.1109/jproc.2010.2043918.

Fausto, R.S., van As, D., Mankoff, K.D., Vandecrux, B., Citterio, M., Ahlstrøm, A.P., Andersen, S.B., Colgan, W., Karlsson, N.B., Kjeldsen, K.K., Korsgaard, N.J., Larsen, S. H., Nielsen, S., Pedersen, A.Ø., Shields, C.L., Solgaard, A.M., Box, J.E., 2021. Programme for Monitoring of the Greenland Ice Sheet (PROMICE) automatic weather station data. Earth Syst. Sci. Data 13, 3819–3845. https://doi.org/10.5194/essd-13-3819-2021.

Fettweis, X., Gallée, H., Lefebre, F., et al., 2006. The 1988–2003 Greenland ice sheet melt extent using passive microwave satellite data and a regional climate model. Clim. Dyn. 27, 531–541. https://doi.org/10.1007/s00382-006-0150-8.

Greene, C.A., Gwyther, D.E., Blankenship, D.D., 2017. Antarctic mapping tools for Matlab. Comput. Geosci. 104, 151–157. https://doi.org/10.1016/j.cageo.2016.08.003. Elsevier BV.

Harper, J., Humphrey, N., Pfeffer, W.T., Brown, J., Fettweis, X., 2012. Greenland ice-sheet contribution to sea-level rise buffered by meltwater storage in firn. Nature 491 (7423), 240–243. https://doi.org/10.1038/nature11566.

Houtz, D., Naderpour, R., Schwank, M., Steffen, K., 2019. Snow wetness and density retrieved from L-band satellite radiometer observations over a site in the West Greenland ablation zone. Remote Sens. Environ. 235, 111361.

Houtz, D., Mätzler, C., Naderpour, R., Schwank, M., Steffen, K., 2021. Quantifying surface melt and liquid water on the Greenland ice sheet using L-band radiometry. Remote Sens. Environ. 256, p. 112341). https://doi.org/10.1016/j.rse.2021.112341.

Howat, I.M., Negrete, A., Smith, B.E., 2014. The Greenland ice mapping project (GIMP) land classification and surface elevation data sets. Cryosphere 8 (4), 1509–1518.

Imaoka, K., Kachi, M., Fujii, H., Murakami, H., Hori, M., Ono, A., Igarashi, T., Nakagawa, K., Oki, T., Honda, Y., Shimoda, H., 2010. Global change observation Mission (GCOM) for monitoring carbon, water cycles, and climate change. IEEE Proc. 98 (5), 717–734.

Jezek, K.C., Johnson, J.T., Tan, S., Tsang, L., Andrews, M.J., Brogioni, M., Macelloni, G., Durand, M., Chen, C.-C., Belgiovane, D.J., Duan, Y., Yardim, C., Li, H., Bringer, A., Leuski, V., Aksoy, M., 2018. 500–2000-MHz brightness temperature spectra of the northwestern Greenland ice sheet. IEEE Trans. Geosci. Remote Sens. 56 (3), 1485–1496. https://doi.org/10.1109/tgrs.2017.2764381.

Jezek, K.C., Merry, C.J., Cavalieri, D.J., 1993. Comparison of SMMR and SSM/I passive microwave data collected over Antarctica. A. Glaciology. 17, 131–136. https://doi.org/10.1017/S0260305500012726.

Leduc-Leballeur, M., Picard, G., Macelloni, G., Mialon, A., Kerr, Y.H., 2020. Melt in Antarctica derived from Soil Moisture and Ocean Salinity (SMOS) observations at L band. The Cryosphere 14, 539–548. https://doi.org/10.5194/tc-14-539-2020.

Mecklenburg, S., Drusch, M., Kaleschke, L., Rodriguez-Fernandez, N., Reul, N., Kerr, Y., Font, J., Martin-Neira, M., Oliva, R., et al., 2016. ESA's soil moisture and ocean salinity mission: from science to operational applications. Remote Sens. Environ. 180, 3–18. https://doi.org/10.1016/j.rse.2015.12.025.

Miller, J.Z., Long, D.G., Jezek, K.C., Johnson, J.T., Brodzik, M.J., Shuman, C.A., Koenig, L.S., Scambos, T.A., 2020. Brief communication: mapping Greenland's perennial firn aquifers using enhanced-resolution L-band brightness temperature image time series. Cryosphere 14 (9), 2809–2817. https://doi.org/10.5194/tc-14-2809-2020.

Miller, J.Z., Culberg, R., Long, D.G., Shuman, C.A., Schroeder, D.M., Brodzik, M.J., 2022a. An empirical algorithm to map perennial firn aquifers, ice slabs, and perched firn aquifers within the Greenland ice sheet using satellite L-band microwave radiometry. Cryosphere 16, 103–125. https://doi.org/10.5194/tc-16-103-2022.

Miller, J.Z., Long, D.G., Shuman, C.A., Culberg, R., Hardman, M.A., Brodzik, M.J., 2022. Mapping firn saturation over Greenland using NASA's soil moisture active passive satellite. IEEE J. Select. Top. Appl. Earth Observ. Remote Sens. 15, 3714–3729. https://doi.org/10.1109/JSTARS.2022.3154968, 2022.

Mote, T.L., Anderson, M.R., 1995. Variations in snowpack melt on the Greenland ice sheet based on passive-microwave measurements. J. Glaciology 41 (137), 51–60.

Mousavi, M., Colliander, A., Miller, J.Z., Entekhabi, D., Johnson, J.T., Shuman, C.A., Kimball, J.S., Courville, Z.R., 2021. Evaluation of surface melt on the Greenland ice sheet using SMAP L-band microwave radiometry. IEEE J. Sel. Topics Appl. Earth Obs. Remote Sens. 14, 11439–11449. https://doi.org/10.1109/jstars.2021.3124229.

Mousavi, M., Colliander, A., Miller, J.Z., Kimball, J., 2022. A novel approach to map the intensity of surface melting on the Antarctica ice sheet using SMAP L-band microwave radiometry. IEEE J. Sel. Topics Appl. Earth Observ. Remote Sens. 15, 1724–1743.

Naderpour, Reza, Schwank, Mike, Mätzler, Christian, 2017. Davos-laret remote sensing field laboratory: 2016/2017 winter season L-band measurements data-processing and analysis. Remote Sens. 9 (11), 1185.

Naderpour, Reza, Schwank, Mike, 2018. Snow wetness retrieved from L-band radiometry. Remote Sens. 10 (3), 359.

Naderpour, R., Houtz, D., Schwank, M., 2021. Snow wetness retrieved from close-range L-band radiometry in the western Greenland ablation zone. J. Glaciology 67 (261), 27–38. https://doi.org/10.1017/jog.2020.79.

Oerlemans, J., Vugts, H.F., 1993. A meteorological experiment in the melting zone of the Greenland ice sheet. Bull. Am. Meteorol. Soc. 74 (3), 355–366.

Piepmeier, J.R., Focardi, P., Horgan, K.A., Knuble, J., Ehsan, N., Lucey, J., Brambora, C., Brown, P.R., Hoffman, P.J., French, R.T., Mikhaylov, R.L., Kwack, E.-Y., Slimko, E. M., Dawson, D.E., Hudson, D., Peng, J., Mohammed, P.N., De Amici, G., Freedman, A.P., Njoku, E.G., 2017. SMAP L-band microwave radiometer: instrument design and first year on orbit. IEEE Trans. Geosci. Remote Sens. 55 (4), 1954–1966. https://doi.org/10.1109/tgrs.2016.2631978.

Samimi, S., Marshall, S.J., MacFerrin, M., 2020. Meltwater penetration through temperate ice layers in the percolation zone at DYE-2, Greenland ice sheet. Geophys. Res. Lett. 47, e2020GL089211 https://doi.org/10.1029/2020GL089211.

Samimi, S., Marshall, S.J., Vandecrux, B., MacFerrin, M., 2021. Time-domain reflectometry measurements and modeling of firn meltwater infiltration at DYE-2, Greenland. J.Geophys.Rese.Earth Surf. https://doi.org/10.1029/2021jf006295.

Schwank, Mike, Naderpour, Reza, 2018. Snow density and ground permittivity retrieved from L-band radiometry: melting effects. Remote Sens. 10 (2), 354.

Smeets, P.C.J.P., Kuipers Munneke, P., van As, D., van den Broeke, M.R., Boot, W., Oerlemans, H., Snellen, H., Reijmer, C.H., van de Wal, Roderik S.W., 2018. The K-transect in West Greenland: automatic weather station data (1993–2016). Arct. Antarct. Alp. Res. 50 (1), S100002. https://doi.org/10.1080/15230430.2017.1420.

Snyder, J.P., 1987. Map Projections–A Working Manual, vol. 1395. US Government Printing Office, Washington, DC.

Steffen, K., Abdalati, W., Stroeve, J., 1993. Climate sensitivity studies of the Greenland ice sheet using satellite AVHRR, SMMR, SSM/I and in situ data. Meteorl. Atmos. Phys. 51 (3–4), 239–258. https://doi.org/10.1007/BF01030497.

Tedesco, M., 2007. Snowmelt detection over the Greenland ice sheet from SSM/I brightness temperature daily variations. Geophys. Res. Lett. Vol. 34, No. L02504 https://doi.org/10.1029/2006GL028466.

Tedesco, M., 2009. Assessment and development of snowmelt retrieval algorithms over Antarctica from K-band spaceborne brightness temperature (1979–2008). Remote Sens. Environ. 113, 979–997.

Tedesco, M., 2015. Remote sensing of the cryosphere. In: Tedesco, M. (Ed.), The Cyrosphere Science Series. Wiley Blackwell, Hoboken, NJ, USA, 2015; ISBN 978-1-118-36885-5.